Acta Pharmaceutica Sinica B 2022;12(2):952–966

Chinese Pharmaceutical Association
Institute of Materia Medica, Chinese Academy of Medical Sciences

Acta Pharmaceutica Sinica B

www.elsevier.com/locate/apsb
www.sciencedirect.com

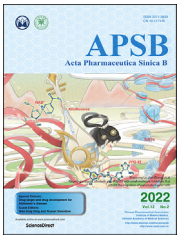

ORIGINAL ARTICLE

Structurally defined tandem-responsive nanoassemblies composed of dipeptide-based photosensitive derivatives and hypoxia-activated camptothecin prodrugs against primary and metastatic breast tumors

Mengchi Sun[a], Hailun Jiang[b], Tian Liu[a], Xiao Tan[a], Qikun Jiang[a], Bingjun Sun[b], Yulong Zheng[c], Gang Wang[d], Yang Wang[d], Maosheng Cheng[b], Zhonggui He[a,*], Jin Sun[a,*]

[a]*Wuya College of Innovation, Shenyang Pharmaceutical University, Shenyang 110016, China*
[b]*Key Laboratory of Structure-Based Drug Design and Discovery, Shenyang Pharmaceutical University, Ministry of Education, Shenyang 110016, China*
[c]*School of Materials Science and Engineering, Ocean University of China, Qingdao 266100, China*
[d]*College of Pharmacy, Guangxi University of Chinese Medicine, Nanning 530200, China*

Received 10 April 2021; received in revised form 10 May 2021; accepted 28 May 2021

KEY WORDS

Chemo-photodynamic;
Tandem-responsive;
Both-in-one co-nanoassembly;
Computational simulations;
Camptothecin;
Pyropheophorbide;
Reactive oxygen species;
Breast tumor metastasis

Abstract Substantial progress in the use of chemo-photodynamic nano-drug delivery systems (nano-DDS) for the treatment of the malignant breast cancer has been achieved. The inability to customize precise nanostructures, however, has limited the therapeutic efficacy of the prepared nano-DDS to date. Here, we report a structurally defined tandem-responsive chemo-photosensitive co-nanoassembly to eliminate primary breast tumor and prevent lung metastasis. This both-in-one co-nanoassembly is prepared by assembling a biocompatible photosensitive derivative (pheophorbide-diphenylalanine peptide, PPA-DA) with a hypoxia-activated camptothecin (CPT) prodrug [(4-nitrophenyl) formate camptothecin, N-CPT]. According to computational simulations, the co-assembly nanostructure is not the classical core-shell type, but consists of many small microphase regions. Upon exposure to a 660 nm laser, PPA-DA induce high levels of ROS production to effectively achieve the apoptosis of normoxic cancer cells. Subsequently, the hypoxia-activated N-CPT and CPT spatially penetrate deep into the hypoxic

*Corresponding authors. Tel./fax: +86 24 23986321.
E-mail addresses: hezhonggui@vip.163.com (Zhonggui He), sunjin@syphu.edu.cn (Jin Sun).

Peer review under responsibility of Chinese Pharmaceutical Association and Institute of Materia Medica, Chinese Academy of Medical Sciences.

https://doi.org/10.1016/j.apsb.2021.08.008

region of the tumor and suppress hypoxia-induced tumor metastasis. Benefiting from the rational design of the chemo-photodynamic both-in-one nano-DDS, these nanomedicines exhibit a promising potential in the inhibition of difficult-to-treat breast tumor metastasis in patients with breast cancer.

1. Introduction

Breast cancer seriously threatens the health of women around the world and the high mortality rate of breast cancer in the clinic is largely due to tumor metastasis[1,2]. Hypoxia, a common feature of tumors, has been discovered to be a key driver of metastasis[3]. Camptothecin (CPT), a classical nuclear DNA topoisomerase I (TOP1) inhibitor, reversibly binds at the interface of the TOP1−DNA complex, resulting in TOP1-mediated DNA damage. It has been also reported to inhibit the expression of intracellular hypoxia-inducing factor-1α (HIF1α), subsequently reducing the hypoxia-associated tumor metastasis[4]. However, the clinical efficacy of CPT is poor for the following reasons: i) the poor solubility and instability of CPT; ii) the poor vasculature and condensed extracellular matrix (ECM) of tumors; and iii) the non-selective distribution and systematic toxicity of CPT[5,6]. Nano-drug delivery systems (nano-DDS) are capable of improving the stability and enhancing the tumor-targeting efficiency of drugs[7−11]. However, given the poor vasculature and ECM of tumors, the ability of nano-DDSs to reach the deep hypoxic region of the tumor is still limited.

Photodynamic therapy (PDT) utilizes the photosensitizer (PS)-triggered production of cytotoxic reactive oxygen species (ROS) under near-infrared (NIR) laser irradiation to kill tumor cells[12−16]. Despite the noninvasive characteristics and superior selectivity, PDT-induced O_2 consumption aggravates tumor hypoxia and limits its beneficial therapeutic outcomes. Accordingly, the application of PDT in combination with hypoxia-activated chemotherapy might make better use of the aggravated hypoxia environment induced by PDT to concurrently bio-activate hypoxia-based prodrugs[17−20]. The previous study by Feng et al.[21] provided proof of principle for the application of a multipurpose liposome encapsulating a hypoxia-activated prodrug (AQ4N) and a PS (hCe6) as a theranostic nanomedicine[21].

A remaining challenge is how to build the well-designed high-loading co-delivery nano-DDS composed of chemotherapeutics and PS. Recently, researchers have focused on the computational simulation of the design and optimization of various formulations[22−24]. The simulation models provide insights into the assembly dynamics and the structures of formulations at the molecular level[22]. As a typical example, Shi et al.[23] disclosed the high binding affinity between a rhein-containing nanocarrier and doxorubicin (Dox) using a computational simulation-based high throughput assay. Moreover, as shown in our recent study, the simulation-assisted diphenylalanine (FF)-modified prodrug nanoassembly effectively encapsulates CPT and exhibits favorable antitumor efficacy[24].

In this study, we develop a well-defined chemo-photodynamic nanoplatform to treat primary and metastatic breast tumors using the combination of computational simulations and experiments. This facile design incorporates the following elements: i) PS-FF conjugates for good mono-assembly and biocompatibility; ii) molecule-matching nanostructures that combine PS derivative and the hypoxia-activated CPT prodrug; and iii) cooperative both that potentially produce high concentration ROS upon laser irradiation, then bio-activate the N-CPT in tandem. The main mechanism underlying the inhibition of tumor metastasis was that CPT released from N-CPT spatially penetrated the hypoxic core of the tumor to inhibit HIF1α expression. Our findings provide opportunities for the computation-aided development of a structurally precise both-in-one co-nanoassembly DDS as an anti-tumor metastasis agent.

2. Materials and methods

2.1. Materials

CPT was purchased from Dalian Meilun Biotech Co., Ltd. The (4-nitrophenyl) formate was obtained from Shanghai Energy Chemical Co., Ltd., Shanghai, China. Pyropheophorbide (PPA) was purchased from Shanghai Dibai Chemical Technology Co., Ltd., Shanghai, China. The phenylalanine-phenylalanine-glycine tripeptide was obtained from Zhejiang Ontores Biotechnologies Co., Ltd., Hangzhou, China. A cellular ROS Detection assay kit (DCFH-DA) were obtained from Dalian Meilun Biotech Co., Ltd., Dalian, China. Cell culture media RPMI 1640, Dulbecco's modified Eagle's medium (DMEM), penicilline−streptomycin and fetal bovine serum were purchased from GIBCO, Carlsbad, USA. 3-(4,5-Dimthyl-2-thiazolyl)-2,5-dipphenyl-2*H*-terazolium bromide (MTT) and trypsin-EDTA were obtained from Sigma–Aldrich, USA. 1,2-Distearoyl-*sn*-glycero-3-phosphoethanolamine-*N*-[methoxy(polyethyleneglycol)-2000] (DSPE-PEG_{2K}) was purchased from Shanghai Advanced Vehicle Technology Co., Ltd. Other chemicals and solvents used in the present study were analytical or HPLC grade.

2.2. Synthesis of dipeptide-based photosensitive derivatives and hypoxia-responsive camptothecin prodrugs

The pheophorbide (0.64 g, 1.2 mmol) was dissolved in 3 mL ultra-dry DMF. HATU (0.46 g, 1.2 mmol), DIPEA (0.16 g, 1.2 mmol) and phenylalanine-phenylalanine- glycine (0.37 g, 1.0 mmol) were added to the reaction. The reaction mixture was stirred at room temperature for 5 h. At the end of the reaction, 10 mL of saturated sodium bicarbonate was added to the reaction solution, solid was gradually precipitated from the reaction solution. The residues were extracted by ethyl acetate three times (20 mL × 3), washed by clean water, saturated salt water and dried with anhydrous sodium sulfate. The solid crude product was purified by silica gel column chromatography with petroleum ether: ethyl acetate = 10:1 to 1:1, black solid was obtained with a yield of 71.2%, ESI-MS *m/z*: 886.4 $[M+H]^+$, ^{1}H NMR (600 MHz,

DMSO-d_6) δ 9.73 (s, 1H), 9.44 (s, 1H), 8.90 (s, 1H), 8.22 (dd, J = 17.8, 11.6 Hz, 1H), 8.17 (d, J = 8.4 Hz, 1H), 8.14 (t, J = 5.9 Hz, 1H), 7.42 (d, J = 6.7 Hz, 1H), 7.14 (d, J = 6.8 Hz, 2H), 7.10 (d, J = 7.5 Hz, 2H), 7.07 (d, J = 5.2 Hz, 2H), 7.06 (s, 2H),7.04 − 6.94 (m, 2H), 6.39 (dd, J = 17.8, 1.4 Hz, 1H), 6.21 (dd, J = 11.6, 1.3 Hz, 1H), 5.22 (d, J = 19.6 Hz, 1H), 5.11 (d, J = 19.5 Hz, 1H), 4.61 − 4.53 (m, 1H), 4.31 (dd, J = 22.1, 9.1 Hz, 2H), 3.95 (q, J = 5.8 Hz, 1H), 3.70 (q, J = 7.9 Hz, 2H), 3.66 (d, J = 5.8 Hz, 2H), 3.61 − 3.55 (m, 2H), 3.43 (s, 3H), 3.22 (s, 3H), 3.16 (d, J = 3.6 Hz, 1H), 3.04 (dd, J = 13.3, 5.2 Hz, 1H), 2.95 (dd, J = 14.0, 4.2 Hz, 1H), 2.87 (dd, J = 13.3, 5.8 Hz, 1H), 2.66 (dd, J = 13.9, 9.8 Hz, 1H), 2.57 (s, 1H), 2.44 (dd, J = 14.4, 8.2 Hz, 1H), 2.11 (t, J = 12.0 Hz, 2H), 1.76 (d, J = 7.3 Hz, 3H), 1.62 (t, J = 7.6 Hz, 3H), 1.22 (s, 3H).

The 4-nitrophenyl chloroformate (0.24 g, 1.2 mmol) was dissolved in 3 mL ultra-dry DMF. TEA (0.12 g, 1.2 mmol) and camptothecin (0.35 g, 1.0 mmol) were added to the reaction. The reaction mixture was stirred at room temperature for 5 h. At the end of the reaction, 10 mL of saturated sodium bicarbonate was added to the reaction solution, solid was gradually precipitated from the reaction solution. The residues were extracted by ethyl acetate three times (20 mL × 3), washed by clean water, saturated salt water and dried with anhydrous sodium sulfate. The solid crude product was purified by silica gel column chromatography with petroleum ether: ethyl acetate = 10:1 to 1:1 and solid was obtained with a yield of 60.8%, ESI-MS m/z: 536.9$[M+Na]^+$, ^{1}H NMR (600 MHz, DMSO-d_6) δ 8.73 (s, 1H), 8.31 − 8.28 (m, 2H), 8.20 (d, J = 7.9 Hz, 1H), 8.16 (d, J = 8.4 Hz, 1H), 7.89 (ddd, J = 8.4, 6.8, 1.5 Hz, 1H), 7.74 (ddd, J = 8.1, 6.8, 1.2 Hz, 1H), 7.55 − 7.51 (m, 2H), 7.28 (s, 1H), 5.62 − 5.51 (m, 2H), 5.33 (d, J = 2.2 Hz, 2H), 2.28 (dt, J = 12.4, 7.1 Hz, 2H), 0.97 (t, J = 7.4 Hz, 3H).

2.3. Preparation and characterization of the both-in-one co-nanoassembly

The both-in-one co-nanoassembly was prepared using a reported nano-precipitation method[8,9,25]. Briefly, PPA-DA and N-CPT were dissolved in a certain amount of DMSO, the organic solution was added gently into deionized water under mechanical stirring (900–1000 rpm). The both-in-one co-nanoassembly was formed spontaneously. The PEGylated co-nanoassembly was produced by mixing both prodrugs with DSPE-PEG_{2000} in water (DSPE-PEG_{2000}/PPA-DA = 15/100, w/w). A solution of co-nanoassembly was transferred to ultracentrifugation (Millipore, MWCO 100 kDa) and centrifuged at 2000×g for 10 min, during which deionized water was replaced for three times. The particle size and zeta potential of co-nanoassemblies were measured by dynamic light scattering (DLS) using a Zetasizer (Nano ZS, Malvern Co., UK). The drug loading (DL) was determined by the ultracentrifugation method and calculated as following Eq. (1):

$$\mathrm{DL}(\%) = \text{Weight of drug in co-nanoassembly} / \text{Total weight of co-nanoassembly} \times 100 \quad (1)$$

The drug-loading content of PPA-DA and N-CPT was measured to be 89.5% and 10.4% (w/w), respectively. The particle size and morphology of the co-nanoassembly were also determined using Transmission electron microscopy (TEM) (JEOL 100CX II, Japan). The prepared co-nanoassembly was dropped onto copper wire meshes and stood for 2 min. Next, the excess liquid was removed. Grids were stained with 2% phosphotungstic acid for 2 min and dried by the infrared lamp.

2.4. Computational simulation

All computational experiments were conducted on a Dell PowerEdge R900 workstation under the RHEL 5.3 platform. The chemical structures were constructed using Sybyl 6.9.1 (Tripos Inc.). The energy minimization was conducted: Powell method (Tripos force field), Gasteiger−Hückel charges, the Steepest Descent algorithm, the Conjugate Gradient and Adopted Basis Newton-Raphson algorithms with an energy change of 0.005 kcal/mol•A or Max Iterations 10,000. The molecular docking studies were performed by using Discovery Studio 3.0 software package. The relevant parameter of docking was described in our past work[18]. The lowest binding energy of each complex was shown in Supporting Information Table S2, and its corresponding binding mode was analyzed using Discovery Studio Visualizer 2017.

The dissipative particle dynamics (DPD) simulations were performed using the Material Studio 2017 software package. The multi-atom grouped together and formed a single bead called a DPD bead. The motion of all beads would follow the Newton's second law. In this paper, DPD simulations attempted to build the co-nanoassemblies between PPA-DA and N-CPT in aqueous solution. The single PPA-DA molecule contained two beads, and so did the N-CPT. Three H_2O molecules were grouped into one H_2O bead. The relative amount of the bead was PPA-DA:water:N-CPT = 9:1000:1. This was agreed well with our experimental conditions. The solubility parameter and the interaction parameters were shown in Supporting Information Tables S4 and S5. Similar to our previous study, the size of the box was 100 × 100 × 100 Å[18]. The system temperature remained constant at 297 K in a 75-ns run in the NVT ensemble.

2.5. Cellular uptake

The 4T1 cells were seeded in 24-well plate at a density of 5×10^4 cells per well and cultured for 24 h. Then the cells were incubated with the co-nanoassemblies for 1, 4, 12 or 24 h. Afterwards, discarding the medium and rinsing three times with cold PBS. The fluorescence signals of PPA-DA were collected using a confocal laser scanning microscopy (CLSM, Nikon Corp., Tokyo, Japan).

Flow cytometry was used to quantify intracellular uptake of PPA-DA from the co-nanoassemblies. 4T1 cells were incubated in 24-well plate (5×10^4 cells/well) for 24 h, then the cells were treated with the co-nanoassemblies for 1, 4, 12 or 24 h, respectively. Subsequently, the cells were rinsed with cold PBS thrice and treated with trypsin. Then the cells were harvested by centrifugation and resuspended with 300 μL PBS. The fluorescence signal of N-CPT was measured by flow cytometer (FACSCalibur, BD Biosciences, San Jose,CA, USA).

2.6. Cytotoxicity

The cytotoxicity of CPT and N-CPT against 4T1 cells was evaluated using MTT assay under the normoxic environment. 4T1 cells (7×10^3 cells per well) were seeded into 96-well plates prior to treatment of drugs. After pre-treatment for 24 h, cancer cells were treated with serial dilutions of CPT and N-CPT, further incubated for 24 h. Untreated cells were chosen as control. At the end of the incubation, 150 μL of MTT (1 mg/mL) was added to

each well for another 4 h at 37 °C. The medium was then discarded and replaced with 150 μL DMSO, and the absorbency of the medium solution was measured on a microplate reader at 490 nm. Each concentration was tested in three wells and all data were shown as mean ± SD.

To explore the hypoxia-activated anti-cancer efficacy, cells were pre-treated with $CoCl_2$ (a chemical inducer of hypoxia, 10 mmol/L) for 24 h, and further incubated with CPT and N-CPT in the presence of $CoCl_2$ for 24 h before viability assessment *via* the MTT assay. To simulate the hypoxic condition, the plates of treatment groups were incubated in a low oxygen environment before viability assessment using anaerobic gas producting bag (QingDao Hopebio-Technology Co., Ltd., Tsingtao, China).

To evaluate the *in vitro* synergetic anti-cancer efficacy, PPA-DA mono-nanoassemblies, N-CPT, PPA-DA mono-nanoassemblies plus laser and co-nanoassemblies plus laser (the same concentration of N-CPT as the co-nanoassemblies) were incubated with 4T1 cells in 96-well plates at various final concentrations of N-CPT at 37 °C for 12 h. Cells were irradiated with specific wavelength laser (660 nm, 20 mW/cm^2) for 3 min, and further incubated for 12 h before viability assessment by the MTT assay.

2.7. Intracellular CPT release

We determined the release of CPT from N-CPT, co-nanoassemblies or co-nanoassemblies under the laser irradiation after incubation with 4T1 cells. Briefly, 4T1 cells were seeded in 12-well plates at a density of 1×10^5 cells per well and incubated for 24 h. Then, cells were washed and incubated with N-CPT, co-nanoassemblies or co-nanoassemblies under the laser irradiation for 4 h at 37 °C ($n = 3$). After incubation, cells were washed and irradiated with 660 nm laser (20 mW/cm^2) for 3 min. The cells together with the drug-containing PBS were collected, and the cells were broken by ultrasonication. The concentrations of free CPT in the solutions were determined by S6000 HPLC (Acchrom, Beijing, China).

2.8. In vitro singlet oxygen detection and oxygen consumption

The production of singlet oxygen in 4T1 cells was detected by a DCFH-DA Reagent Kit. 4T1 cells (at 7×10^3 cells per well) were seeded in 96-well plates for 24 h. Subsequently, medium containing PPA-DA mono-assemblies, PPA-DA & CPT co-assemblies, and PPA-DA & N-CPT co-assemblies were added to the cells for 24 h. After the medium was displaced with DCFH-DA (10 μg/mL) for 30 min, the cells were irradiated by a 660 nm laser device (20 mW/cm^2). Finally, the Eclipse Ti-U inverted microscope was used to detect singlet oxygen production in 4T1 cells. In addition, PSs could react irreversibly with O_2 to cause a reduction under the laser irradiation (20 mW/cm^2, 3 min). Briefly, control, PPA-DA mono-nanoassemblies with/without 660 nm laser and co-nanoassemblies with/without 660 nm laser (20 μg/mL PPA-DA) were added to aqueous solution (3 mL). The dissolved O_2 in above mixture was measured using a JPB-607A portable dissolved oxygen meter (INESA, China).

2.9. The wound healing assay

The inhibitory effect of the formulations on migration 4T1 cells was measured by the wound healing assay. The 10^5/well cells were seeded into 12-well plate and allowed to grow to 90%−95% confluency. The confluent monolayer was scraped with a sterile 200 μL pipette tip to form a cell-free zone. Then, cells were incubated with co-nanoassemblies (at equivalent dose of N-CPT of 10 ng/mL), PPA-DA mono-nanoassemblies and N-CPT (10 ng/mL) for the wound healing assay. The 12-well plates were under the 660 nm laser irradiation at 20 mW/cm^2 for 3 min.

2.10. Animal studies

The BALB/c mice were obtained the Laboratory Animal Center of Shenyang Pharmaceutical University (Shenyang, China) at 6–8 weeks (18–20 g) of age. All mice were housed in a specific pathogen-free environment at a constant temperature (22 ± 3 °C), with a 12 h light/dark cycle and fed adaptively for 1 week after arrival. During the experiments, mice had free access to water and were fed the maintenance diet (Yuhong Qianmin Foodstuffs Corporation, Shenyang, China). All animals received humane care and experimental protocols were carried out in accordance with the Guidelines for the Care and Use of Laboratory Animals, as approved by the Institutional Animal Ethical Care Committee of Shenyang Pharmaceutical University.

2.11. Biodistribution, pharmacokinetics and ROS generation in vivo

The subcutaneous breast cancer xenograft bearing 4T1 female BALB/c mice was employed to evaluate the biodistribution of the co-nanoassemblies. 4T1 cells (5×10^6 cells) were injected into the right flanks of female BALB/c mice. The mice bearing cancer cells were divided into two groups ($n = 3$). The Dir-labeled co-nanoassemblies and free Dir at 2 mg Dir/kg were administrated intravenously when the tumor volume reached around 300 mm^3. Fluorescence imaging was performed at different time intervals (3, 6, 9, 12, and 24 h) post i.v. injection using IVIS imaging system. At post 9 h injection, the mice were sacrificed and the fluorescence imaging in the major organs (heart, liver, spleens, lungs, and kidneys) and tumors were analyzed by the *in vivo* imaging system (IVIS) ($n = 3$).

The female BALB/c mice were also carried out the *in vivo* pharmacokinetic studies. The mice were randomly divided into two groups ($n = 3$). The co-nanoassemblies and free N-CPT were intravenously administrated with a dose of 2 mg N-CPT/kg. 500 μL blood samples were collected from vena ophthalmica at the pre-determined times and centrifuged for 10 min at the speed of 12,000×g immediately to obtain plasma. The concentration of N-CPT from the co-nanoassemblies and free N-CPT in plasma was determined by a microplate reader. In addition, more precise tumor accumulation was investigated by determination of the concentration of CPT from N-CPT, co-nanoassemblies or co-nanoassemblies under the laser irradiation in above obtained tumors using S6000 HPLC (Acchrom, China).

To evaluate laser-mediated ROS generation *in vivo*, the BALB/c mice bearing tumor were i.v. injected with co-nanoassemblies (equivalent to 2 mg/kg of N-CPT). After 9 h post co-nanoassemblies systematic injection, the 4T1-bearing mice were exposed to laser (660 nm, 100 mW/cm^2) for 5min. The tumors were locally injected with ROS probe DCFH-DA 20 min before irradiation. The tumor tissues were collected to analyze the ROS generation in tumors by inverted fluorescence microscope after the irradiation.

2.12. The synergistic anti-tumor activity in vivo

To investigate the targeting behavior of nanoassemblies, 4T1 subcutaneous tumor-bearing female BALB/c mice were employed. The subcutaneous breast cancer xenografts were established by injecting

5×10^6 4T1 cells into the right flank of the female BALB/c mice ($n = 5$). When the tumor size reached an average volume of around 100 mm^3, the animals received tail vein injections of the various drug formulations (Control, CPT, N-CPT, PPA-DA mono-nanoassemblies+laser, the co-nanoassemblies+laser) every 2 days for 10 days. These formulations (equivalent to 2 mg/kg CPT) were intravenously administrated every other day for a total of three injections, and the treated laser groups were exposed to laser (660 nm, 100 mW/cm^2) for 5 min. During the treatment, the tumor sizes were calculated using Eq. (2):

$$V = 1/2ab^2 \quad (2)$$

where a is long axis, and b is short axis.

Mice with tumor implants were sacrificed after 10 treatment days, and main organs (heart, liver, spleen, lung, and kidney) and the tumors were collected, weighed and sliced for hematoxylin and eosin (H&E) staining. The orthotopic 4T1 tumor-bearing mice models displayed greater propensity to form many micrometastasis sites within the lung and liver. To verify whether nanoassemblies could efficiently reduce the risk of metastasis, the orthotopic *in vivo* antitumor experimental profiles were conducted. For orthotopic breast cancer xenografts, 5×10^6 4T1 cells were injected into the orthotopic fat pads of female BALB/c mice. The orthotopic *in vivo* antitumor experimental profiles were similar to that of the subcutaneous breast cancer xenografts.

2.13. Immunofluorescence

Tumor sections were washed in PBS and heated with water bath for antigen retrieval[26]. Then, sections were incubated in the goat serum (LOT: 94A00106) to prevent nonspecific binding of IgG for 1 h at room temperature. Next, the primary antibody was applied to the sections at 4 °C overnight. The primary antibodies used in this experiment were HIF1α Rabbit pAb (1:100; ABclonal; LOT: 3560319004). Subsequently, sections were incubated with FITC-coupled secondary antibody (1:100; ABclonal; LOT: 9300011001). The sections were incubated with DAPI, then, the images were taken using an Eclipse Ti-U inverted microscope (Nikon Corp., Tokyo, Japan). The HIF1α colocalization percentage was measured by Image J software.

2.14. Ingenuity pathways analysis between HIF1α and metastasis-related proteins

The ingenuity pathways analysis (IPA) was used to interpret the interactions in the context of biological networks. All HIF1α-associated metastasis proteins were selected in the dataset. Both up- and down-regulated factors were analyzed as value parameters.

2.15. Statistical analysis

Data were calculated and processed as mean ± SD. Comparison between groups was analyzed with Student's t-test (two-tailed) and one-way analysis of variance (ANOVA). Statistical differences were considered significant at $^*P < 0.05$, $^{**}P < 0.01$, $^{***}P < 0.001$[3].

3. Results and discussion

3.1. Synthesis of the FF-based photosensitive derivative and hypoxia-activated camptothecin prodrug

A FF-based photosensitive derivative (PPA-DA) was designed and synthesized by conjugating FF to pheophorbide *via* glycine as a linker. Additionally, a hypoxia-activated camptothecin prodrug (N-CPT) was synthesized by coupling (4-nitrophenyl) formate to the C20′-oxygen of camptothecin (CPT). The synthetic routes are depicted in Supporting Information Scheme S1, and the chemical structures of both compounds are presented as mass spectra in Supporting Information Fig. S1. The ^{1}H NMR spectra and chemical shifts of both compounds were further confirmed in Supporting Information Fig. S2.

3.2. Preparation and characterization of co-nanoassemblies

The FF, an assembly inducer, was the core moiety of the designed PPA-DA[27]. The synthesized PPA-DA formed uniform mono-nanoassemblies with a mean diameter of ~40 nm through a one-step nanoprecipitation method. The nanoassembly was subjected to PEGylation (DSPE-PEG_{2K}) to improve the stability and increase the blood circulation time of the nanomedicines[8,9]. PEGylated mono-nanoassemblies showed an increased particle size (diameter of ~60 nm) (Supporting Information Table S1). No nanoscale particles were measured when the system only contained pheophorbide and DSPE-PEG_{2K}, suggesting that FF was indispensable for the formation of co-nanoassemblies.

Both PPA-DA and N-CPT co-assembled into one nanoassembly using the one-step nanoprecipitation method described above Fig. 1A. When the organic solution of both was added to deionized water, the co-nanoassemblies spontaneously formed. As shown in Fig. 1C, the PEGylated co-nanoassembly exhibited diameters of ~70 nm, according to the dynamic light scattering (DLS) measurements. Transmission electron microscopy (TEM) images (Fig. 1B) revealed a spherical shape of the PEGylated co-nanoassemblies with a size of ~70 nm. As depicted in Fig. 1D, the colloidal stability of the PEGylated co-nanoassemblies in cell culture media (DMEM) was investigated. No significant change was observed when PEGylated co-nanoassemblies were incubated in DMEM at 37 °C for 24 h. Moreover, the PEGylated co-nanoassemblies also exhibited good stability during storage at 4 °C for one week and high colloidal stability under the simulated *in vivo* environment [PBS (pH 7.4) supplemented with 10% FBS at 37 °C for 24 h, Fig. 1E and Supporting Information Fig. S3], which were suitable for further study. Both PPA-DA mono-nanoassemblies and co-nanoassemblies displayed similar UV–Vis absorption spectra at wavelengths ranging from 450 to 900 nm, with the maximum observed at 680 nm (Fig. 1F).

3.3. Determination of co-assembly mechanisms with computational simulations

The interactions between PPA-DA and N-CPT were first analyzed using molecular docking to evaluate the co-assembly mechanism. The results of the molecular docking experiments are shown in Supporting Information Table S2. It was found that the complex between PPA-DA and N-CPT had a lower energy than that between PPA-DA and CPT (Fig. 2A). From the perspective of

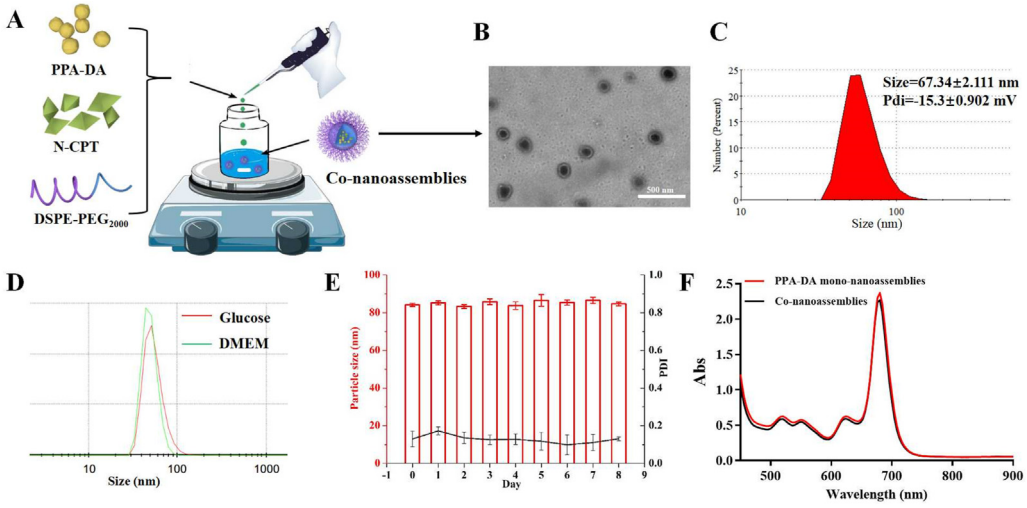

Figure 1 (A) Preparation procedure of the co-nanoassembly formulation. (B) Transmission electron microscopy (TEM) image and (C) Dynamic light scattering (DLS) profile of co-nanoassemblies. (D) DLS profiles of co-nanoassemblies in glucose and in DMEM. Before the characterization, co-nanoassemblies in DMEM were incubated at 37 °C for 24 h. (E) Hydrodynamic diameters of co-nanoassemblies at 4 °C during one week. (F) UV–Vis absorption spectra of PPA-DA mono-nanoassemblies and co-nanoassemblies.

thermodynamics, the PPA-DA & N-CPT complex with a low energy represented a favorable stable system compared to the PPA-DA & CPT complex[23]. Based on the aggregation-caused quenching (ACQ) of intrinsic fluorescence by PSs, we further attempted to understand the mechanisms underlying the interactions of N-CPT or CPT with PPA-DA using an experimental tool[28]. The insertion of the N-CPT or CPT molecules into PPA-DA mono-assembly disturbed the aggregation of photosensitizers (PSs) and partially restored the ACQ effect of PSs. The N-CPT & PPA-DA complex exhibited lower fluorescence signals than the CPT & PPA-DA complex (Fig. 2B), suggesting that N-CPT matched better with PPA-DA, consistent with the docking results. The fluorescence intensity of both complex (N-CPT & PPA-DA and CPT & PPA-DA) under various concentrations had been quantified (Supporting Information Fig. S4), also in line with the docking results. Moreover, PSs would generate singlet oxygen under laser irradiation. The singlet oxygen generation capacity of the PPA-DA mono-assemblies, PPA-DA & CPT co-assemblies and PPA-DA & N-CPT co-assemblies was investigated by using a DCFH-DA Reagent Kit. The laser-activated PPA-DA mono-assemblies displayed quenched photodynamic activity due to compact $\pi-\pi$ stacking interactions. The singlet oxygen generation of PPA-DA & CPT co-assemblies was a bit stronger than that of the PPA-DA & N-CPT co-assemblies (Supporting Information Fig. S5).

According to our previous report, the flexible bond angle promotes the assembly process and improves the stability of nanoassemblies[25]. Here, we also calculated the bond angles

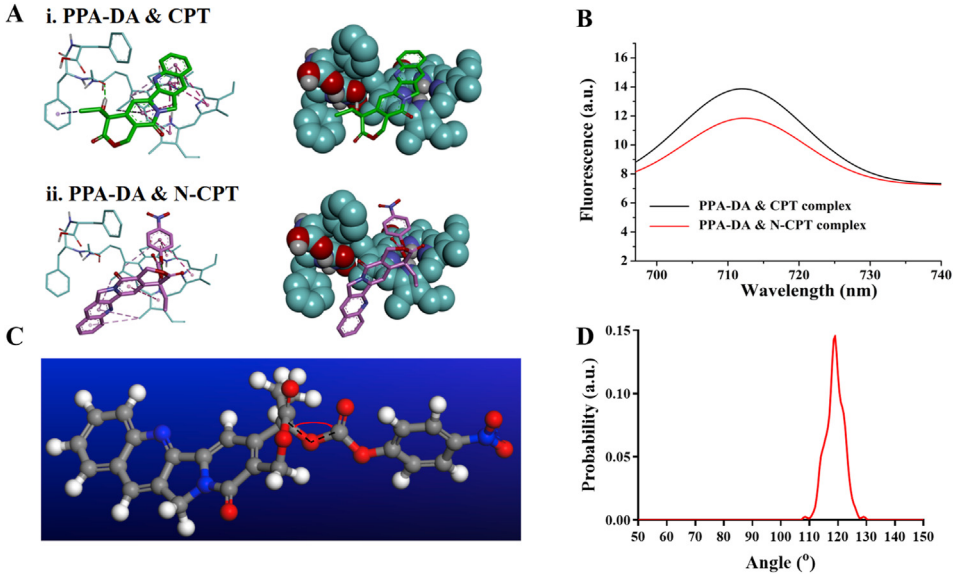

Figure 2 (A) The interactions of three dimensional chemical structures between i) CPT and PPA-DA, and ii) N-CPT and PPA-DA. The oxygen atoms are red. The carbon atoms are green. The pink imaginary lines represent $\pi-\pi$ stacking interactions. (B) Fluorescence emission spectra of PPA-DA & N-CPT complex and PPA-DA & CPT complex. (C) The bond angle of −C20′−O−C− in N-CPT. (D) The bond angle probability of N-CPT between (4-nitrophenyl) formate and CPT.

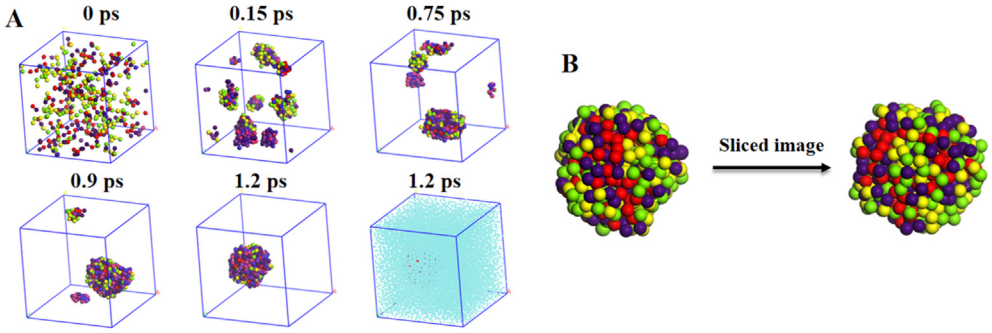

Figure 3 (A) The co-nanoassembly progression of PPA-DA and N-CPT. The periodic images of the system are shown. Water has been shown in the last image. (B) Final nanostructure and the cross-sectional view of one co-nanoassembly.

between (4-nitrophenyl)formate and CPT using molecular dynamic (MD) simulations (Fig. 2C). The bond angle of −C20′-−O−C− in N-CPT rotated continually at angles ranging from 110° to 130° during the MD process (Fig. 2D). Compared to the rigid and planar structure of CPT, the conformation flexibility of N-CPT favored the dynamic co-assembly with PPA-DA.

Next, dissipative particle dynamics (DPD) simulations were conducted to reveal the co-assembly mechanism (Supporting Information Fig. S6)[29]. The snapshots displayed the co-assembly process at various time intervals (Fig. 3A). The N-CPT&PPA-DA complexes gradually aggregated into many small co-assemblies from the initial random state, and finally formed a single large co-assembly. The conformation of the single large co-assembly and the sliced image of this co-assembly are shown in Fig. 3B. The co-assembly did not form the classical core-shell type of structure, but consisted of many small microphase regions. The morphologies revealed how N-CPT and PPA-DA co-assembled into a large co-assembly. Additional representative TEM images of co-nanoassemblies at higher magnification were provided Supporting Information Fig. S7.

3.4. In vitro cellular uptake and cytotoxicity of co-nanoassembly

We initially investigated the cellular uptake of the co-nanoassembly. The co-nanoassemblies were incubated with 4T1 cells for 1, 4, 12 or 24 h. The intracellular fluorescence intensity of PPA-DA from co-nanoassemblies was observed using confocal laser scanning microscopy (CLSM), and the intracellular uptake of PPA-DA was quantitatively measured using flow cytometry. As presented in Fig. 4, the co-nanoassemblies showed a time-dependent increase in cellular uptake, and higher intracellular amounts of co-nanoassemblies were observed.

The hypoxia-activated cytotoxicity of N-CPT was evaluated under normoxic/hypoxic conditions using the standard cell viability (MTT) assay[20–32]. As shown in Fig. 5A, N-CPT exerted stronger antitumor effect in the hypoxia than that in the normoxic environment, and the IC_{50} value of N-CPT was obviously decreased to 2.92 μg/mL under the hypoxic condition compared to the normoxic condition (14.15 μg/mL). The result verified the selective cytotoxicity of the hypoxia-activated N-CPT prodrug under normoxic/hypoxia conditions (Supporting Information Fig. S8).

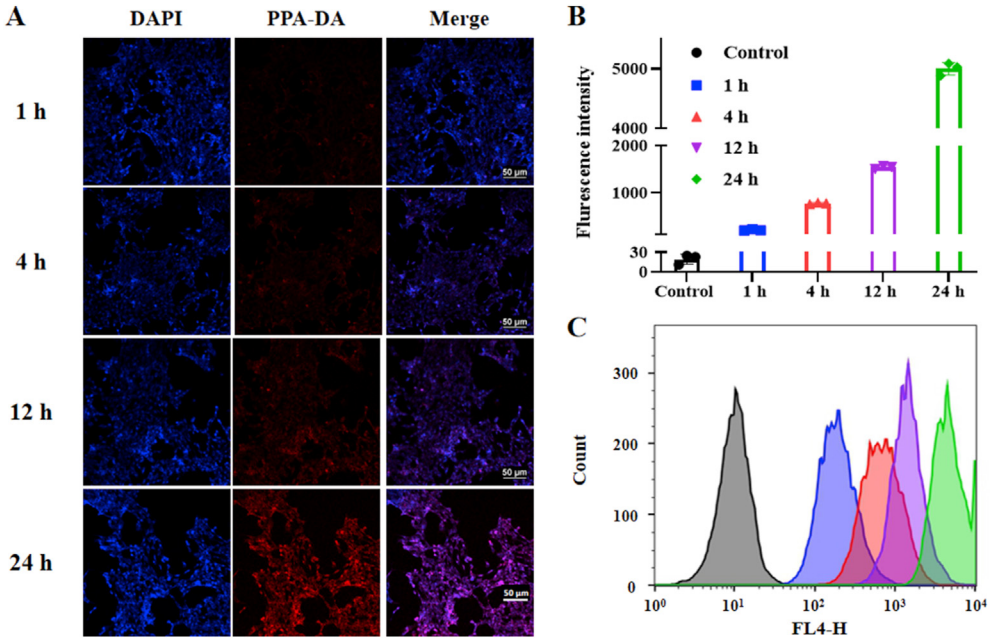

Figure 4 (A) Confocal fluorescence images of 4T1 cells incubation with co-nanoassemblies (at equivalent dose of N-CPT of 10 ng/mL) for 1, 4, 12 or 24 h. Scale bar = 50 μm. (B) and (C) Cellular uptake behavior of PPA-DA from co-nanoassemblies at 1, 4, 12 or 24 h analyzed by flow cytometer.

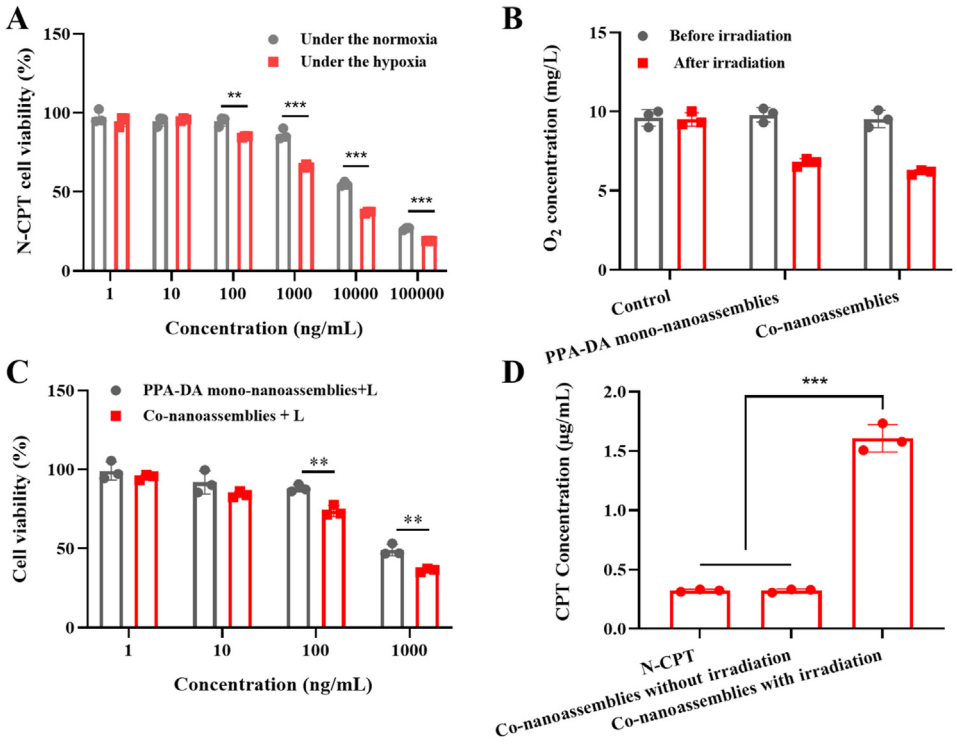

Figure 5 (A) Cytotoxicity of N-CPT within the normoxia or hypoxia ($n = 3$). (B) O_2 concentration determinations of control, PPA-DA mono-nanoassemblies and co-nanoassemblies (20 μg/mL PPA-DA) after 660 nm laser irradiation (20 mW/cm^2) for 3 min ($n = 3$). (C) Cytotoxicity of PPA-DA mono-nanoassemblies and co-nanoassemblies ($n = 3$). (D) CPT released from co-nanoassemblies with/without the laser irradiation (20 mW/cm^2) for 3 min after cellular uptake in 4T1 cells for 4 h ($n = 3$). *$P < 0.05$, **$P < 0.01$, ***$P < 0.001$ by two-tailed Student's t-test.

In this study, we introduced hypoxia-responsive *p*-aminobenzyl groups into camptothecin prodrug (N-CPT). It has been reported that the *p*-nitrobenzyl groups could be bioreduced to *p*-aminobenzyl groups by over-expressed nitroreductase in hypoxic cells and undergo spontaneous fragmentation, resulting in hypoxia-responsive drug release[33]. To better illustrate the idea, the visual plots of electrostatic potential (ESP) displayed that the surface charge (represented by blue arrows) of the N-CPT to be from −5.49 (–NO_2) to 5.49 e^{-2} (–NH_2) under the hypoxia-induced bio-reducing microenvironment in Supporting Information Fig. S9. When nitro group was reduced to amino group, the negative potential of O_1−C_2 (represented by red arrows) had been augmented. Since oxygen atoms with strong electron-withdrawing ability were substituted for hydrogen atoms, the charges were induced to other oxygen atoms such as O_1, O_2 and O_3. The enlargement of negative potential of O_1 and O_2−C_2−O_3 group resulted in the enhancement of repulsion interaction between them which extended O_1−C_2 bond length and diminished its bond energy. These results would facilitate to release the active compound (CPT) in Fig. S8.

Moreover, the oxygen concentrations were measured after laser irradiation for 3 min using a portable dissolved oxygen meter. As illustrated in Fig. 5B, the O_2 concentration was further decreased after irradiation. The photodynamic PPA-DA generated further anabatic hypoxia for N-CPT activation. Then, the hypoxia-activated cytotoxicity of the chemotherapy-PDT combination was investigated in 4T1 cells. The cytotoxicity of the irradiation without co-nanoassemblies was shown in Supporting Information Fig. S10, demonstrating that irradiation conditions did not have any influence in the 4T1 cells. Upon irradiation with 660 nm light, the PPA-DA mono-nanoassembly efficiently killed cancer cells (IC_{50} 0.35 μg/mL). Pretreatment of cells with co-nanoassemblies resulted in the reduced IC_{50} values (IC_{50} 0.22 μg/mL), indicating the effective anti-tumor efficacy of the combination of N-CPT and PPA-DA (Fig. 5C). In addition, the CPT conversion behavior from co-nanoassemblies was investigated after 4T1 cells were or were not exposed to laser irradiation. Fig. 5D showed the lack of a significant difference between the N-CPT solution and co-nanoassemblies without irradiation. The co-nanoassemblies with irradiation showed nearly 5-fold higher CPT concentrations than co-assemblies without irradiation.

3.5. *Anti-metastasis efficiency of co-nanoassemblies in vitro*

Since cancer cell migration is directly related to the tumor metastasis, we evaluated the inhibitory effects of different formulations (Control, N-CPT, PPA-DA mono-nanoassemblies+laser and co-nanoassemblies+laser) on cell migration using wound healing trials. The 4T1 cells, a highly metastatic murine cell line, was chosen as a model cell line. As shown in Fig. 6A, the wound gap had nearly disappeared in the control group after 24 h. Compared to the N-CPT and PPA-DA mono-nanoassembly groups, cell migration was significantly inhibited in the co-nanoassembly-treated group. The wound healing ratio was quantified in Supporting Information Fig. S11. This result suggested the substantial anti-metastasis effect of the co-nanoassemblies under 660 nm irradiation. Besides, a traditional migration and invasion assay was conducted to evaluate the migration activity of 4T1 cells (Fig. 6B and Supporting Information Fig. S12). Similar to results of the wound healing experiment, the anti-metastasis

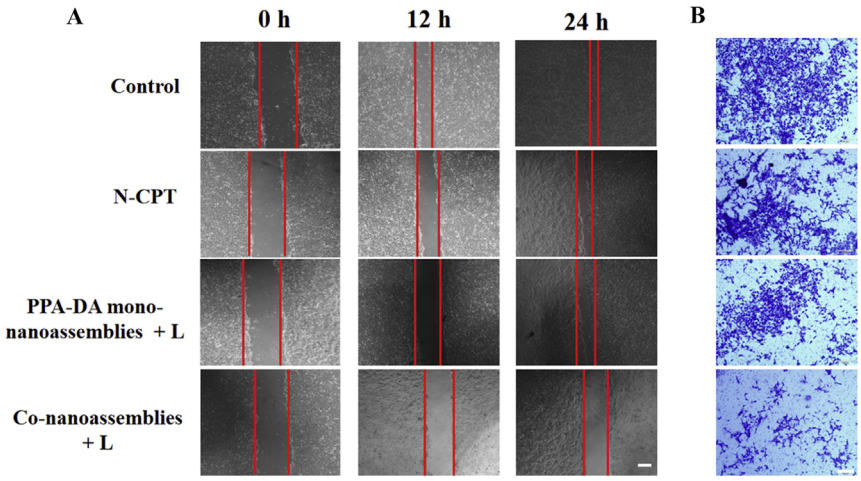

Figure 6 Typical images of (A) wound healing assessments (scale bar: 200 μm) and (B) traditional migration and invasion assays (scale bar: 100 μm) of control, N-CPT, PPA-DA mono-nanoassemblies and co-nanoassemblies under 660 nm irradiation in 4T1 cells.

ability of co-nanoassemblies make it a promising candidate for further *in vivo* evaluation.

3.6. Biodistribution and pharmacokinetics of co-nanoassemblies in vivo

Prior to the biodistribution experiment, the fluorescence resonance energy transfer (FRET) effect between Dir and PPA-DA was investigated. As depicted in Supporting Information Fig. S13, the Dir fluorescent signal in a solution containing a mixture of Dir and PPA-DA exhibited little change compared to free Dir, suggesting no involvement of the FRET effect between Dir and PPA-DA. The BALB/c mice bearing 4T1 tumor xenografts were established to evaluate the biodistribution of the Dir-labeled co-nanoassemblies. The particle size and size distribution of DiR-labeled co-nanoassemblies did not significantly change compared with the previous co-nanoassemblies (Supporting Information Fig. S14). The *in vivo* fluorescence images revealed a noticeably stronger fluorescence intensity of Dir-labeled co-nanoassemblies than free Dir at different time points. The fluorescence of co-nanoassemblies still remained high in the tumor at 24 h, while only a little fluorescence from free Dir was observed (Fig. 7A). At 6 h after the

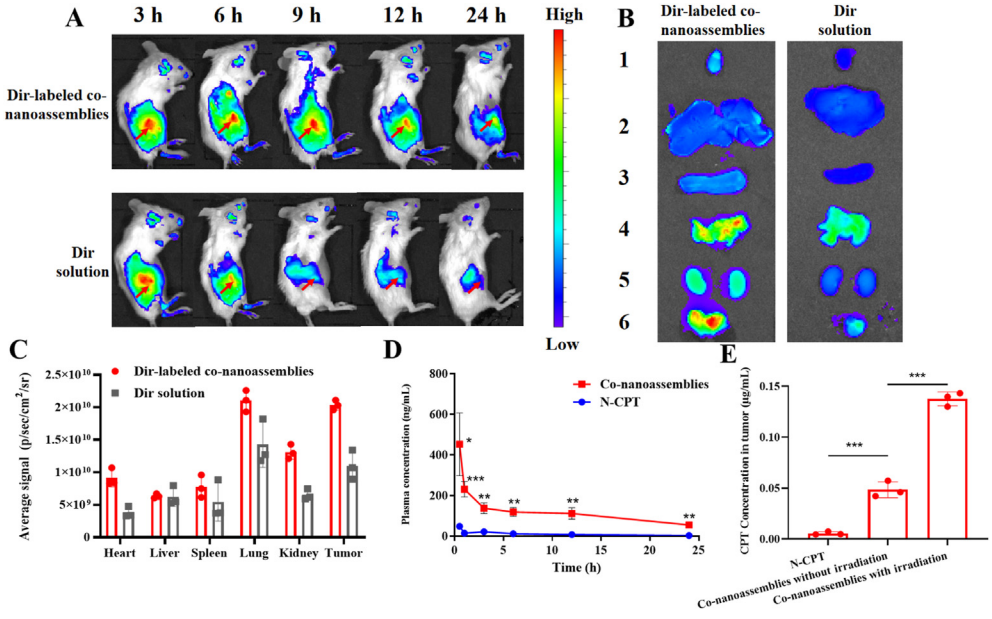

Figure 7 *In vivo* biodistribution of DiR-labeled co-nanoassemblies. (A) *In vivo* fluorescence imaging of 4T1 tumor-bearing mice at 3, 6, 9, 12, and 24 h after i.v. injection of free DiR or DiR-labeled co-nanoassemblies (DiR 2 mg/kg). Arrows refer to the tumor regions. (B) *Ex vivo* fluorescence imaging of excised tumors and major organs at 9 h after i.v. injection from top to bottom (1, heart; 2, liver; 3, spleen; 4, lung; 5, kidney; 6, tumor). (C) Biodistribution levels of DiR in tumors and major organs at 9 h after i.v. injection ($n = 3$). (D) Drug concentration in blood as a function of time after a single intravenous administration of co-nanoassemlies or N-CPT at a N-CPT-equivalent dose of 2 mg/kg ($n = 3$, $^{*}P < 0.05$). (E) Tumor accumulation of CPT with/without irradiation. Data are presented as mean ± SD ($n = 3$). $^{*}P < 0.05$, $^{**}P < 0.01$, $^{***}P < 0.001$ by two-tailed Student's *t*-test.

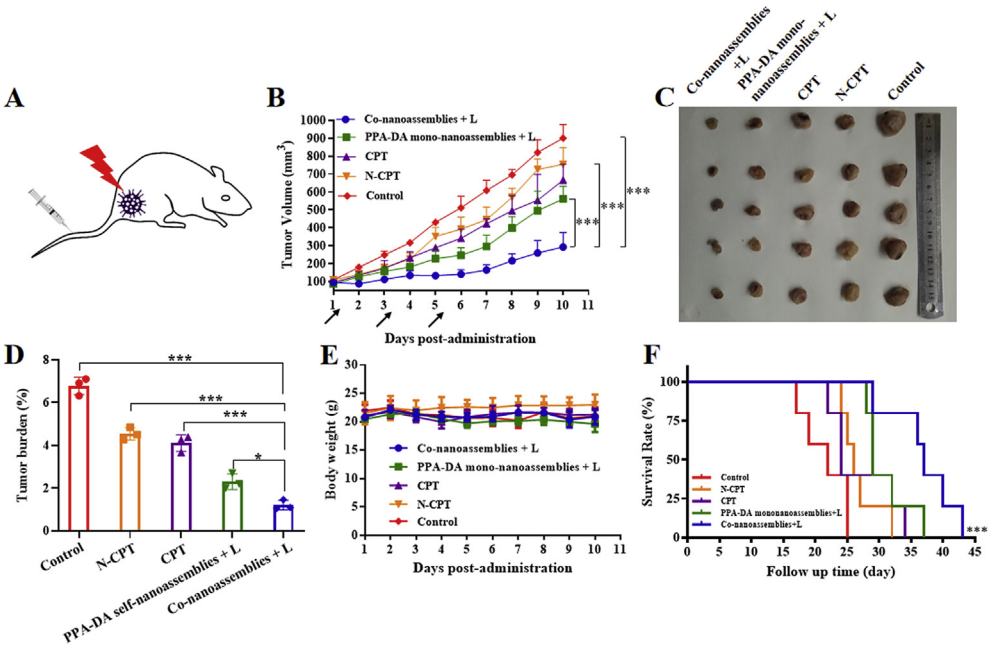

Figure 8 (A) Therapeutic protocol on mouse 4T1 subcutaneous tumor xenograft. (B) Growth curve of the tumor volume after various treatments (the injector represents drug administration). (C) Graphs of tumors after 11 days. (D) The tumor burden of mice during various treatments after 11 days. (E) The body weight changes of mice during various treatments. (F) The survival curves of mice harboring 4T1 tumor xenografts after various treatments. Data presented are the means ± SD, $n = 5$, $^{*}P < 0.05$, $^{**}P < 0.01$, $^{***}P < 0.001$ by two-tailed Student's *t*-test.

injection, the major organs and the tumor tissues were harvested to further quantitatively analyze the biodistribution using spectrofluorimetry (Fig. 7B). As shown in Fig. 7C, the co-nanoassemblies mainly accumulated in the lung, kidney and tumor. The level of the Dir-labeled co-nanoassemblies that accumulated in the tumor was 1.85-fold higher than free Dir.

The effect of the co-nanoassemblies on the pharmacokinetics was studied by intravenously injecting the co-nanoassemblies and free N-CPT (Fig. 7D), and the pharmacokinetic parameters are illustrated in Supporting Information Table S3. The N-CPT from co-nanoassemblies showed a notably prolonged circulation time compared to free N-CPT. The good colloidal stability contributed

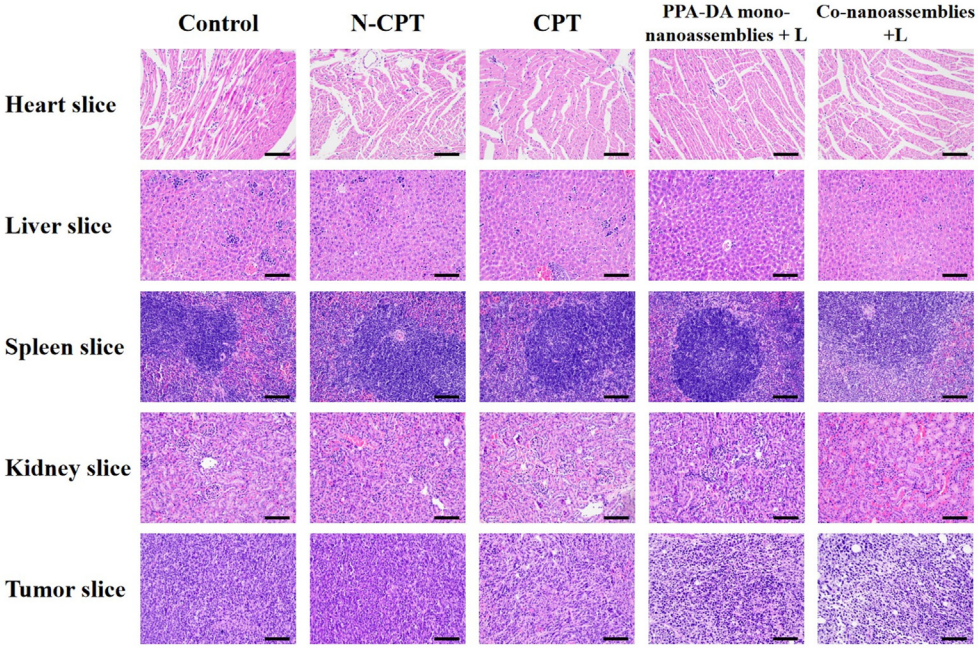

Figure 9 H&E staining images in organs after the treatment with control, N-CPT, CPT, PPA-DA mono-nanoassemblies+L, and co-nanoassemblies+L, scale bar represents 100 μm.

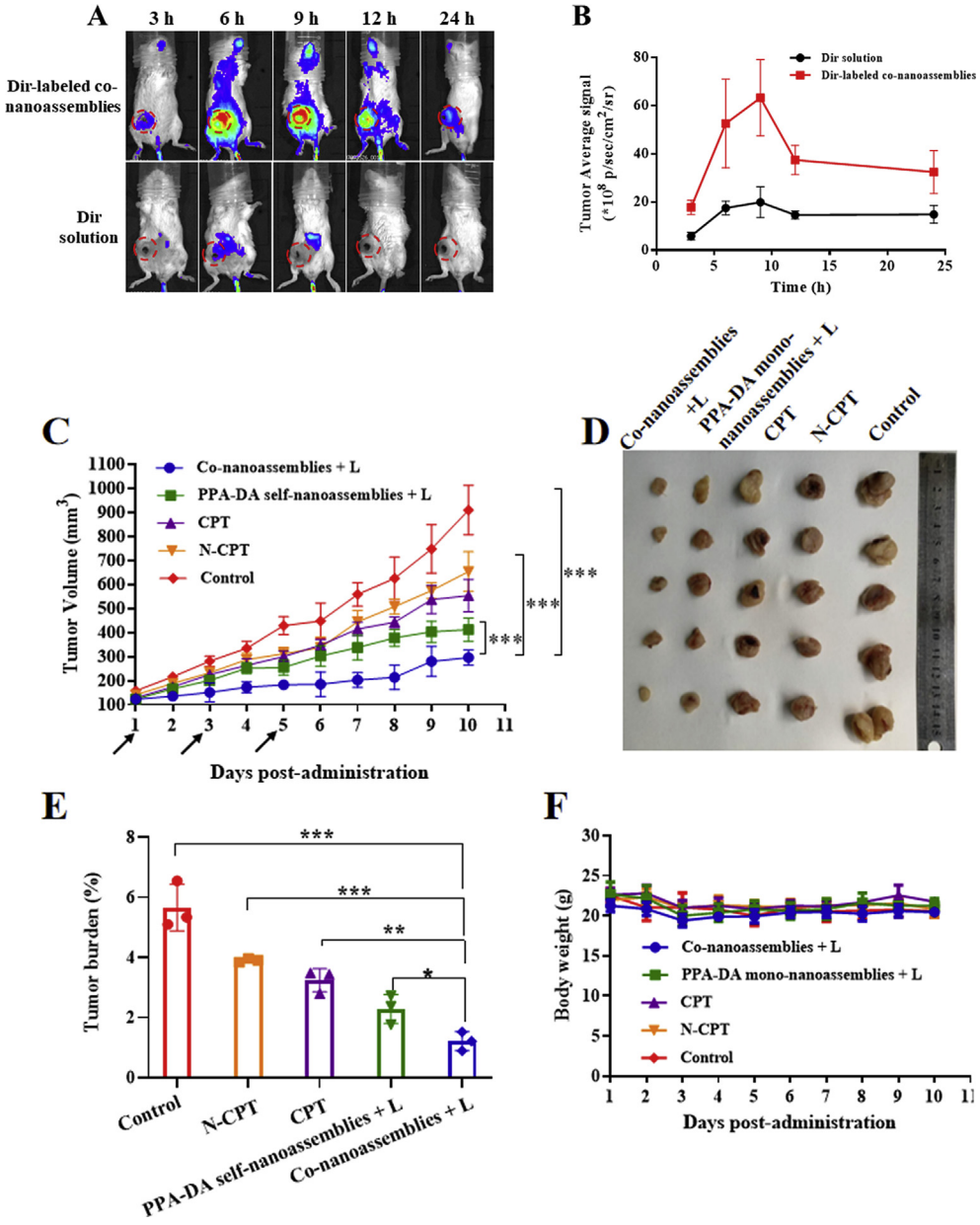

Figure 10 (A) and (B) *In vivo* behavior, fluorescence imaging and intensity of tumor at 24 h post injection of 4T1 orthotopic breast cancer models. (C) Growth curve of the tumor volume after various treatments (the injector represents drug administration). (D) Graphs of tumors after 11 days. (E) The tumor burden of mice during various treatments after 11 days. (F) The body weight changes of mice during various treatments. Data presented are the means ± SD, $n = 5$, $^{*}P < 0.05$, $^{**}P < 0.01$ and $^{***}P < 0.001$ by two-tailed Student's *t*-test.

to the longer systematic circulation time of the co-nanoassemblies than free N-CPT, consistent with the biodistribution behavior. As shown in Fig. 7E, a much higher concentration of CPT derived from co-nanoassemblies was determined in tumors than the group treated with N-CPT solution using the HPLC method, mainly due to the favorable pharmacokinetic behavior of co-nanoassemblies. Upon exposure to a 660 nm laser, a high level of PPA-DA-activated hypoxia was produced. Subsequently, a greater number of hypoxia-activated N-CPT molecules were bio-converted to CPT molecules. To measure laser-triggered ROS production *in vivo*, 9 h post co-nanoassemblies systematic injection, the 4T1-bearing mice were exposed to laser (660 nm, 100 mW/cm^2) for 5 min. DCFH-DA, a ROS kit, was intratumorally injected 20 min before irradiation. The tumors were collected and washed immediately after the irradiation. The immunofluorescence revealed that the fluorescent intensity of ROS probe under the co-nanoassemblies treatment was significantly detected as shown in Supporting Information Fig. S15.

3.7. *In vivo anti-tumor efficacy*

The female BALB/c mice bearing subcutaneous 4T1 xenografts (Fig. 8A) were randomly divided into five groups: control, CPT, N-CPT, PPA-DA mono-nanoassemblies+L (irradiated with a 660 nm laser), and co-nanoassemblies+L (irradiated with a 660 nm laser, five animals per group, $n = 5$). As presented in Fig. 8B, the control group showed a rapid increase in the tumor volume (~900 mm^3 on Day 10). The free CPT and free N-CPT groups displayed a moderate tumor

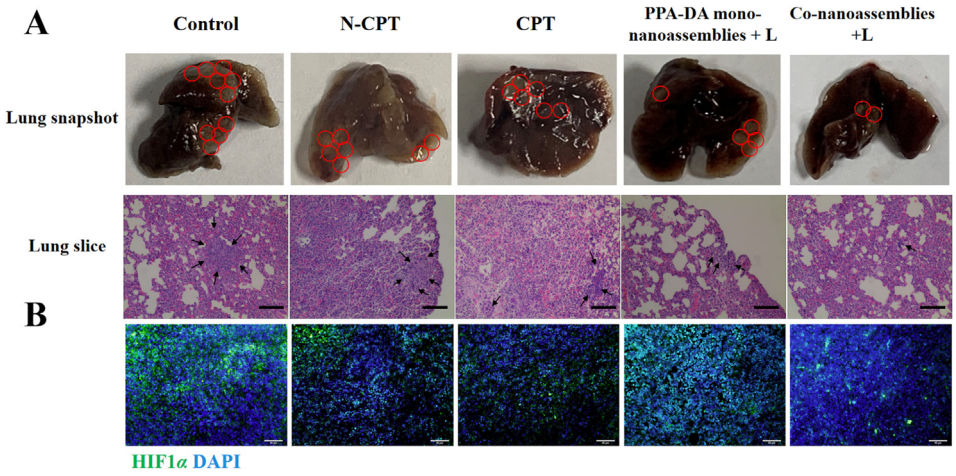

Figure 11 (A) Photos of whole lungs and H&E staining of the lung slices collected from different groups of mice after various treatments on mouse 4T1 subcutaneous tumor xenograft, scale bar represents 100 μm. (B) Representative immunofluorescence analyses of HIF1α from tumor sections. FITC-labeled HIF1α antibody (green), and cell nuclei were stained with 4′,6-diamidino-2-phenylindole (DAPI, blue). Scale bar = 50 μm.

inhibitory capability, but the tumor volumes still reached ~600 and ~700 mm^3 on Day 10, respectively. The poor efficacy of free drugs was ascribed to poor the pharmacokinetic characteristics (Fig. 7D). Additionally, PPA-DA mono-nanoassemblies and co-nanoassemblies exhibited better tumor inhibitory effects than the other groups. The growth of tumors in the co-nanoassemblies group was reduced compared with the PPA-DA mono-nanoassemblies group, indicating a synergistic antitumor effect of the combination of PDT and hypoxia-activated drugs. After Day 11, the tumor tissues were collected and weighed. The lowest average weight of the tumors was observed in the co-nanoassemblies group, consistent with the growth curve (Fig. 8D). The survival curves of the mice suggested that the best synergistic cancer therapy ability of co-nanoassemblies *in vivo* (Fig. 8F).

We also assessed the safety of different formulations after treatments (Fig. 8E). A notable change in body weight was not observed among all groups. The H&E staining of major organ sections did not reveal noticeable histological deficiencies, confirming the negligible treatment-induced toxicity of the formulations to the major organs (Fig. 9).

To further investigate the anti-tumor effects *in vivo*, orthotopic breast cancer models were established by orthotopically injecting 4T1 cells into the fat pads of female BALB/c mice. First, we conducted to the biodistribution experiment in this model. Compared to the Dir solution, the Dir-labeled co-nanoassemblies showed a higher accumulation in the tumor and the largest amount of accumulation amount at 9 h (Fig. 10A and B). Like the subcutaneous models, the anti-tumor activity of co-nanoassemblies in the orthotopic model was better than the other groups (Fig. 10). The *in vivo* anti-tumor results of both breast cancer models evidently confirmed the safety and synergistic therapeutic outcomes of the co-nanoassemblies (Supporting Information Fig. S16).

3.8. *Anti-metastasis evaluation in vivo*

We compared the therapeutic outcomes of different formulations (Control, CPT, N-CPT, PPA-DA mono-nanoassemblies+L, and co-nanoassemblies+L) to elucidate the ability of the hypoxia-activated combination chemotherapy-PDT therapy to inhibit 4T1 tumor metastasis. The inhibitory effect on metastasis was determined using by visualizing the lung tissues with the naked eye and performing H&E staining of the lung tissues. The orthotopic 4T1 models (Supporting Information Fig. S20) formed a larger metastasis area in the lung than mice with subcutaneous xenografts (Fig. 11), suggesting that the orthotopic model was a more highly aggressive tumor model. The chemotherapy (CPT or N-CPT) or PDT (PPA-DA mono-nanoassemblies) inhibited the tumor metastasis to some extent, while the co-nanoassemblies exerted the strongest inhibitory effect on metastasis.

HIF1α plays a key role in the metastasis of cancer cells located in a hypoxic microenvironment. Histological sections of the untreated tumors collected at different tissue depths revealed that the hypoxic region of tumors was mainly located in core region of the tumor (Supporting Information Fig. S17). HIF1α staining of the core region of the tumor was conducted and the average fluorescence intensity of HIF1α in the tumor was quantified to compare the hypoxic region after treatment with the co-nanoassemblies. A significant decrease in HIF1α was observed in tumor samples treated with the co-nanoassemblies compared to the control group (Fig. 11 and Supporting Information Fig. S22). A decrease in HIF1α is clearly desirable.

To consider the binding affinity between CPT and targeting protein topoisomerase-1 (TOP-1), molecular docking was selected for evaluation (shown in Supporting Information Fig. S23). We could observe that CPT was well positioned to the activity site of TOP-1. There were mainly both types of interactions among the binding surface between CPT and TOP-1, including hydrogen bonds and hydrophobic interactions. The bio-activated N-CPT targeted TOP-1, then impaired the expression and activity of the HIF1α protein. The survival curves from clinical data (TCGA) showed that breast cancer patients (BPRC) with low level expression of HIF1α have a longer survival time than patients with high expression (Fig. 12B). Given the key role of the HIF1α protein in the breast cancer treatment, the interactions between HIF1α and metastasis in the biological network were also investigated *via* the ingenuity pathway analysis (IPA). As shown in Fig. 12A, HIF1α was closely linked to various metastasis-related proteins, such as extracellular proteins (TGFA, TNF, MMP9,

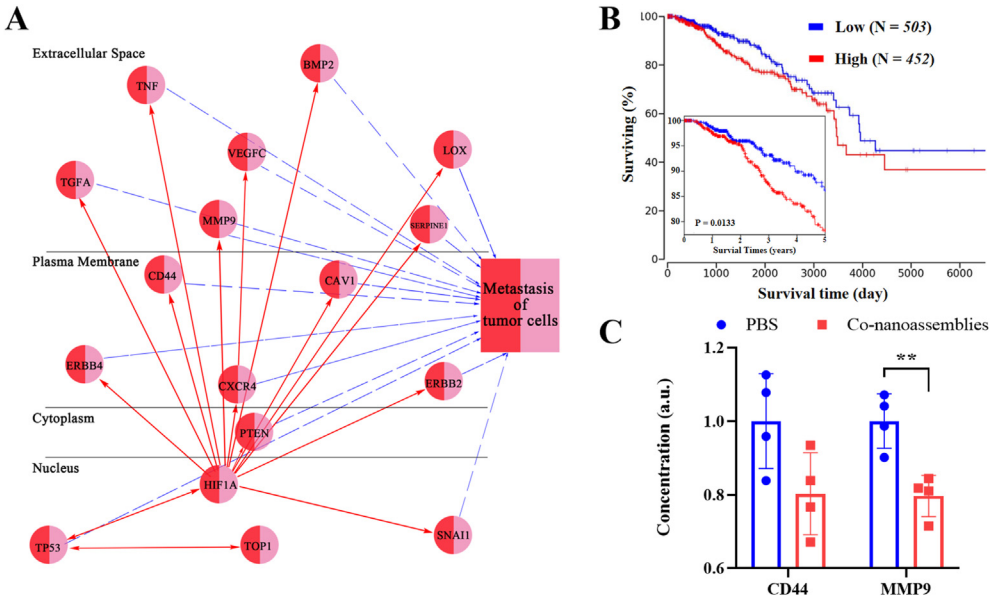

Figure 12 (A) The ingenuity pathway analysis (IPA) image between HIF1α and tumor metastasis in the biological network. (B) Overall and five-year survival curves breast cancer patients (BRCA) with high or low expression of HIF1α, which were obtained from the TCGA (https://ualcan.path.uab.edu/). (C) Intratumoral CD44 and MMP9 level after the PBS or co-nanoassemblies treatment ($n = 4$). Significance between every two groups was calculated using unpaired two-tailed Student's *t*-test. $^{**}P < 0.01$. Data are mean ± SD.

VEGFC, BMP2, SERPINE1, and LOX), membrane proteins (ERBB 4, CD44, CXCR 4, CAV 1, and ERBB2), cytoplasic proteins (PTEN) and nuclear proteins (TP53 and SNAI1)[34–49]. Some of targets (extracellular MMP9 proteins and membrane proteins CD44) shown from IPA analysis had be confirmed by experiments. Substantial downregulation of both metastasis-associated proteins was observed (Fig. 12C). In short, combining the PS-mediated ROS production and hypoxia generated by PDT, the bio-activated N-CPT spatially penetrated the core of the tumor and strongly suppressed HIF1α expression, providing *in vivo* evidence for the synergistic anti-metastasis effects of the both-in-one co-nanoassembly[50].

4. Conclusions

Herein, we fabricated a tandem-responsive both-in-one co-nanoassembly between the FF-based photosensitive derivatives (PPA-DA) and hypoxia-activated camptothecin prodrugs (N-CPT) against breast primary tumor growth and lung metastasis using a computation-aided approach. The computational simulations and the *in vitro* experiments validated that the PPA-DA&N-CPT complex had a favorable binding affinity and formed stable co-nanoassemblies in solution. After systemic administration, the co-nanoassemblies exhibited several significant advantages: i) the co-nanoassemblies exhibited a longer blood circulation time and preferentially accumulated in tumor tissues *via* the EPR effect; ii) upon exposure to laser irradiation, PPA-DA generated a large amount of ROS to kill cancer cells in the normoxic environment. The PDT-induced hypoxic microenvironment bio-activated the N-CPT in tandem, potentiating effective synergistic tumor therapy; iii) the bio-activated CPT could further inhibit the lung metastasis of breast cancer cells by PDT-mediated deeply targeting HIF1α in the tumor core. Taken together, this co-nanoassemblies with the superior antitumor efficiency represent a valuable prospect in the treatment of primary and metastatic breast tumors.

Acknowledgments

This work was supported by National Natural Science Foundation of China, Nos. 81773656 and U1608283; Liaoning Revitalization Talents Program, No. XLYC1808017; Key Projects of Technology Bureau in Shenyang, No. 18400408; Key projects of Liaoning Province Department of Education, No. 2017LZD03; and China Postdoctoral Science Foundation (No. 2020M680986).

Author contributions

Mengchi Sun provided the idea, carried out the experiments, performed the formal analysis, and wrote original draft. Hailun Jiang and Tian Liu took part in the experiment of synthetic compound. Xiao Tan, Qikun Jiang and Bingjun Sun contributed to original writing and editing. Yulong Zheng, Gang Wang, Yang Wang and Maosheng Cheng contributed to formal analysis and diagram drawing. Zhonggui He and Jin Sun provided the funding resources and revised the manuscript. All of the authors have read and approved the final manuscript.

Conflicts of interest

The authors have no conflicts of interest to declare.

Appendix A. Supporting information

Supporting data to this article can be found online at https://doi.org/10.1016/j.apsb.2021.08.008.

References

1. Zhang WJ, Song SC, Wang HX, Wang Q, Li D, Zheng SZ, et al. *In vivo* irreversible albumin-binding near-infrared dye conjugate as a

naked-eye and fluorescence dual-mode imaging agent for lymph node tumor metastasis diagnosis. *Biomaterials* 2019;**217**. 119279-9.
2. Ye H, Wang KY, Wang ML, Liu RZ, Song H, Li N, et al. Bioinspired nanoplatelets for chemo-photothermal therapy of breast cancer metastasis inhibition. *Biomaterials* 2019;**206**:1−12.
3. Wang ML, Zhai YL, Ye H, Lv QH, Sun BJ, Luo C, et al. High co-loading capacity and stimuli-responsive release based on cascade reaction of self-destructive polymer for improved chemo-photodynamic therapy. *ACS Nano* 2019;**13**:7010−23.
4. Semenza G L. Hypoxia-inducible factors: mediators of cancer progression and targets for cancer therapy. *Trends Pharmacol Sci* 2012; **33**:207−14.
5. He D, Zhang W, Deng H, Huo S, Wang YF, et al. Self-assembling nanowires of an amphiphilic camptothecin prodrug derived from homologous derivative conjugation. *Chem Commun* 2016;**52**:14145−8.
6. Wen Y, Wang YZ, Liu XL, Zhang W, Xiong XH, Han ZX, Liang XJ. Camptothecin-based nanodrug delivery systems. Camptothecin-based nanodrug delivery systems. *Cancer Biol Med* 2017;**14**:363−70.
7. Luo C, Sun J, Sun BJ, He ZG. Prodrug-based nanoparticulate drug delivery strategies for cancer therapy. *Trends Pharmacol Sci* 2014: 35556−66.
8. Luo C, Sun J, Liu D, Sun BJ, Miao L, Musetti S, et al. Self-assembled redox dual-responsive prodrug-nanosystem formed by single thioether-bridged paclitaxel-fatty acid conjugate for cancer chemotherapy. *Nano Lett* 2016;**16**:5401−8.
9. Sun BJ, Luo C, Yu H, Zhang XB, Chen Q, Yang WQ, et al. Disulfide bond-driven oxidation- and reduction-responsive prodrug nanoassemblies for cancer therapy. *Nano Lett* 2018;**18**:3643−50.
10. Yue CX, Zhang CL, Alfranca G, Yang Y, Jiang XQ, Yang YM, et al. Near-infrared light triggered ros-activated theranostic platform based on ce6-CPT-ucNPs for simultaneous fluorescence imaging and chemo-photodynamic combined therapy. *Theranostics* 2016;**6**:456−69.
11. Yang Y, Yue C, Han Y, Zhang W, He A, Zhang C, et al. Tumor-responsive small molecule self-assembled nanosystem for simultaneous fluorescence imaging and chemotherapy of lung cancer. *Adv Funct Mater* 2016;**26**:8735−45.
12. Yang B, Wang KY, Zhang D, Sun BJ, Sun J. Light-activatable dual-source ROS-responsive prodrug nanoplatform for synergistic chemo-photodynamic therapy. *Biomater Sci* 2018;**6**:2965−75.
13. Ling DS, Bae B, Park W, Na K. Photodynamic efficacy of photosensitizers under an attenuated light dose *via* lipid nano-carrier-mediated nuclear targeting. *Biomaterials* 2012;**33**:5478−86.
14. Huang ZY, Huang LF, Huang YJ, He YF, Sun XQ, Fu X, et al. Phthalocyanine-based coordination polymer nanoparticles for enhanced photodynamic therapy. *Nanoscale* 2017;**9**:15883−94.
15. Li XS, Yu S, Lee D, Kim G, Yoon J. Facile supramolecular approach to nucleic-acid-driven activatable nanotheranostics that overcome drawbacks of photodynamic therapy. *ACS Nano* 2017;**12**:681−8.
16. Li XS, Fan HH, Guo T, Bai H, Tan W. A sequential protein-responsive nanophotosensitizer complex for enhancing tumor-specific therapy. *ACS Nano* 2019;**13**:6702−10.
17. Ye MZ, Han YX, Tang JB, Piao Y, Liu XR, Zhou ZX, et al. A tumor-specific cascade amplification drug release nanoparticle for overcoming multidrug resistance in cancers. *Adv Mater* 2017;**29**:1702342.
18. Cui D, Huang JG, Zhen X, Li J, Jiang Y, Pu K. A semiconducting polymer nano-prodrug for hypoxia-activated photodynamic cancer therapy. *Angew Chem Int Ed* 2019;**58**:5920−4.
19. Chen L, Revel S, Morris K, C Serpell L, Adams DJ. Effect of molecular structure on the properties of naphthalene-dipeptide hydrogelators. *Langmuir* 2010;**26**:13466−71.
20. Sun YX, Zhao DY, Wang G, Wang Y, Cao LL, Sun J, et al. Recent progress of hypoxia-modulated multifunctional nanomedicines to enhance photodynamic therapy: opportunities challenges and future development. *Acta Pharm Sin B* 2020;**10**:1382−96.
21. Feng LZ, Cheng L, Dong ZL, Tao DL, Barnhart T, Cai W, et al. Theranostic liposomes with hypoxia-activated prodrug to effectively destruct hypoxic tumors post-photodynamic therapy. *ACS Nano* 2017; **11**:927−37.
22. Zhao Y, Fay F, Hak S, Manuel Perez-Aguilar J, Sanchez-Gaytan B, et al. Augmenting drug-carrier compatibility improves tumour nanotherapy efficacy. *Nat Commun* 2016;**7**:11221.
23. Shi CY, Guo DD, Xiao K, Wang X, Wang LL, Luo JT. A drug-specific nanocarrier design for efficient anticancer therapy. *Nat Commun* 2015; **6**. 7449-9.
24. Sun MC, Zhang X, Gao Z, Liu T, Sun J. Probing the dipeptide-based supramolecular assembly as an efficient camptothecin delivering carrier for cancer therapy: computational simulations and experimental validations. *Nanoscale* 2019;**11**:3864−76.
25. Wang YJ, Liu D, Zheng QC, Zhao Q, Zhang HJ, Ma Y, et al. Disulfide bond bridge insertion turns hydrophobic anticancer prodrugs into self-assembled nanomedicines. *Nano Lett* 2014;**14**:5577−83.
26. Zhang Z, Yang JY, Liu C, Xie J, Qiu S, Yang X, et al. Pseudoginsenoside-F11 alleviates cognitive deficits and Alzheimer's disease-type pathologies in SAMP8 mice. *Pharmacol* 2019;**139**: 512−23.
27. Zou Q, Abbas M, Zhao L, Li S, Shen G, Yan X. Biological photothermal nanodots based on self-assembly of peptide−porphyrin conjugates for antitumor therapy. *J Am Chem Soc* 2017;**139**:1921−7.
28. Xiong F, Ling X, Chen X, Chen J, Tan JX, Cao WJ, et al. Pursuing specific chemotherapy of orthotopic breast cancer with lung metastasis from docking nanoparticles driven by bioinspired exosomes. *Nano Lett* 2019;**19**:3256−66.
29. Wang DL, Yu CY, Xu L, Shi LL, Tong GS, Wu JL, et al. Nucleoside analogue-based supramolecular nanodrugs driven by molecular recognition for synergistic cancer therapy. *J Am Chem Soc* 2018;**140**: 8797−806.
30. Li ZQ, Zhu Q, Hu LY, Chen H, Wu ZH, Li D. Anterior gradient 2 is a binding stabilizer of hypoxia inducible factor-1α that enhances $CoCl_2$-induced doxorubicin resistance in breast cancer cells. *Cancer Sci* 2015;**106**:1041−9.
31. He H, Zhu RY, Sun W, Cai KM, Chen YB, Yin LC. Selective cancer treatment *via* photodynamic sensitization of hypoxia-responsive drug delivery. *Nanoscale* 2018;**10**:2856−65.
32. Borenstein X, Fiszman GL, Blidner A, Vanzulli SI, Jasnis MA. Functional changes in murine mammary cancer cells elicited by $CoCl_2$-induced hypoxia. *Nitric Oxide* 2010;**23**:234−41.
33. Zhang P, Yang HL, Shen W, Liu WG, Chen L, Xiao CS. Hypoxia-responsive polypeptide nanoparticles loaded with doxorubicin for breast cancer therapy. *ACS Biomater Sci Eng* 2020;**6**:2167−74.
34. Ravi R, Mookerjee B, Bhujwalla ZM, Sutter CH, Artemov D, Zeng Q, et al. Regulation of tumor angiogenesis by P53-induced degradation of hypoxia-inducible factor 1alpha. *Genes Dev* 2000;**14**: 34−44.
35. Suzuki H, Tomida A, Tsuruo T. Dephosphorylated hypoxia-inducible factor 1α as a mediator of P53-dependent apoptosis during hypoxia. *Oncogene* 2001;**20**:5779−88.
36. Bae MK, Ahn MY, Jeong JW, Bae MH, Lee YM, Bae SK, et al. Jab1 interacts directly with HIF-1alpha and regulates its stability. *J Biol Chem* 2002;**277**:9−12.
37. Senoo M, Matsumura Y, Habu S. TAp63γ (p51A) and dNp63α (p73L) two major isoforms of the p63 gene exert opposite effects on the vascular endothelial growth factor (VEGF) gene expression. *Oncogene* 2002;**21**:2455−65.
38. Hansson LO, Friedler A, Freund S, Rudiger S, Fersht AR. Two sequence motifs from HIF-1alpha bind to the DNA-binding site of p53. *Proc Natl Acad Sci U S A* 2002;**99**:10305−9.
39. Chen D, Li M, Luo J, Gu W. Direct interactions between HIF-1 and Mdm2 modulate p53 function. *J Biol Chem* 2003;**278**:13595−8.
40. Sánchez-Puig N, Veprintsev DB, Fersht AR. Binding of natively unfolded HIF-1alpha ODD domain to p53. *Mol Cell* 2005;**17**: 11−21.
41. Choy MK, Movassagh M, Bennett MR, Foo RS. PKB/Akt activation inhibits p53-mediated HIF1A degradation that is independent of MDM2. *J Cell Physiol* 2010;**222**:635−9.
42. Rohwer N, Dame C, Haugstetter A, Wiedenmann B, Detjen K, Schmitt CA, Cramer T. Hypoxia-inducible factor 1alpha determines

gastric cancer chemosensitivity *via* modulation of p53 and NF-kappaB. *PloS One* 2010;**5**. e12038-8.
43. Zawacka-Pankau J, Grinkevich VV, Hünten S, Nikulenkov F, Gluch A, Li H, et al. Inhibition of glycolytic enzymes mediated by pharmacologically activated p53: targeting Warburg effect to fight cancer. *J Biol Chem* 2011;**286**:41600−15.
44. Chowdhury AR, Long A, Fuchs SY, Rustgi A, Avadhani NG. Mitochondrial stress-induced p53 attenuates HIF-1α activity by physical association and enhanced ubiquitination. *Oncogene* 2017;**36**:397−409.
45. An WG, Kanekal M, Simon MC, Maltepe E, Blagosklonny MV, Neckers LM. Stabilization of wild-type p53 by hypoxia-inducible factor 1alpha. *Nature* 1998;**392**:405−8.
46. Blagosklonny MV, An WG, Romanova LY, Trepel J, Fojo T, Neckers L. p53 inhibits hypoxia-inducible factor-stimulated transcription. *J Biol Chem* 1998;**273**:11995−8.
47. Liu Y, Thor A, Shtivelman E, Cao Y, Tu G, Heath TD, et al. Systemic gene delivery expands the repertoire of effective antiangiogenic agents. *J Biol Chem* 1999;**274**:13338−44.
48. Schito L, Semenza G. Hypoxia-inducible factors: master regulators of cancer progression. *Trends Cancer* 2016;**2**:758−70.
49. Semenza GL. The hypoxic tumor microenvironment: a driving force for breast cancer progression. *Biochim Biophys Acta* 2016;**1863**:382−91.
50. Zhang W, Wang F, Hu C, Zhou Y, Gao HL, Hu J. The progress and perspective of nanoparticle-enabled tumor metastasis treatment. *Acta Pharm Sin B* 2020;**10**:2037−53.